MATERIALS SCIENCE

SINGLE: Atomic-resolution structure identification of nanocrystals by graphene liquid cell EM

Cyril F. Reboul[1,2]*, Junyoung Heo[3,4]*, Chiara Machello[1,2], Simon Kiesewetter[1,2], Byung Hyo Kim[3,4,5], Sungin Kim[3,4], Dominika Elmlund[1,2], Peter Ercius[6], Jungwon Park[3,4]†, Hans Elmlund[1,2]†

Copyright © 2021 The Authors, some rights reserved; exclusive licensee American Association for the Advancement of Science. No claim to original U.S. Government Works. Distributed under a Creative Commons Attribution NonCommercial License 4.0 (CC BY-NC).

Analysis of the three-dimensional (3D) structures of nanocrystals with solution-phase transmission electron microscopy is beginning to reveal their unique physiochemical properties. We developed a "one-particle Brownian 3D reconstruction method" based on imaging of ensembles of colloidal nanocrystals using graphene liquid cell electron microscopy. Projection images of differently rotated nanocrystals are acquired using a direct electron detector with high temporal (<2.5 ms) resolution and analyzed to obtain an ensemble of 3D reconstructions. Here, we introduce computational methods required for successful atomic-resolution 3D reconstruction: (i) tracking of the individual particles throughout the time series, (ii) subtraction of the interfering background of the graphene liquid cell, (iii) identification and rejection of low-quality images, and (iv) tailored strategies for 2D/3D alignment and averaging that differ from those used in biological cryo–electron microscopy. Our developments are made available through the open-source software package SINGLE.

INTRODUCTION

The sustained advances by the crystallographic community over the past 50 years have transformed our understanding of chemistry and biology (*1*). However, numerous targets, including solubilized nanocrystals of fundamental importance to chemical catalysis, remain intractable to traditional crystallographic methods. Colloidal nanocrystals containing a few tens to hundreds of atoms have applications in an ever-expanding range of areas, from electronics to catalysis and biological sensors (*2*). This versatility stems from the high sensitivity of nanocrystal properties to size, chemical composition, and shape, which are largely determined by the synthesis route by which they are produced (*3*, *4*). The structural characteristics of nanocrystals are commonly estimated by a simplistic scale-down picture of the corresponding bulk materials. However, this attempt generally fails because of the unique structural characteristics emerging at the nanoscale. Exposed surfaces, defects, dislocations, and quantum effects are dominant in nanocrystals of finite size (*5*). The ensemble of nanocrystals produced from conventional colloidal synthesis displays a large degree of heterogeneity in the atomic structures, despite the development of synthetic protocols for stringent control of size and morphology (*6*). In addition, the effects of organic ligands and solvent molecules need to be accounted for, since they are important determinants for the surface structures of colloidal nanocrystals (*7*, *8*). Thus, understanding the structures of nanocrystals at a level where fundamental structure-property relationships can be linked requires new analysis methods that allow precise and reproducible determination of the positions of the constituent atoms of single nanocrystals directly from the solution phase.

In typical single-particle three-dimensional (3D) reconstruction, primarily used in structural biology of protein molecules, the molecular Coulomb charge density is reconstructed from tens of thousands projection images of different views of the molecule. The unknown 3D projection angles of the images are determined by sophisticated computational methods (*9*–*14*). Over the past few years, the emergence of a next generation of electron microscopes, with improvement of direct electron detectors, and improved algorithms for image analysis have enabled routine determination of the 3D structures of biological molecules by cryo–electron microscopy (cryo-EM). In favorable cases, it is now possible to determine near-atomic resolution (<4 Å) structures of biomolecules below 100 kDa (*15*) and solve sub-2-Å-resolution structures of larger macromolecules (*16*). However, in situ 3D reconstruction of solubilized individual nanocrystals is an emerging methodology in its early stages of development. We developed SINGLE—a methodology based on independent 3D reconstruction of time series high-resolution transmission EM (HRTEM) images obtained for individual nanocrystals undergoing Brownian motion. SINGLE is the only method developed to date capable of resolving the 3D atomic structures of heterogeneous nanocrystals directly from the solution phase. We here introduce new preprocessing methods for improving the signal-to-noise ratio (SNR) versus the individual movie frames, tracking the particle trajectories, removing graphene-induced background signal, and excluding out-of-focus images. These improved computational methods are required for successful 3D reconstruction from in situ graphene liquid cell (GLC) TEM data. The results presented herein demonstrate the applicability of the SINGLE to obtain atomic-resolution 3D reconstructions of nanocrystals dispersed in solution—samples that would be impossible to image and/or interrogate by any other method.

RESULTS

Overview of SINGLE

The SINGLE suite implements all steps required for obtaining an ensemble of atomic-resolution 3D reconstructions from time series

[1]Department of Biochemistry and Molecular Biology, Biomedicine Discovery Institute, Monash University, Melbourne, Victoria, Australia. [2]Australian Research Council Centre of Excellence in Advanced Molecular Imaging, Monash University, Melbourne, Victoria, Australia. [3]Center for Nanoparticle Research, Institute for Basic Science (IBS), Seoul 08826, South Korea. [4]School of Chemical and Biological Engineering, Institute of Chemical Process, Seoul National University, Seoul 08826, South Korea. [5]Department of Organic Materials and Fiber Engineering, Soongsil University, Seoul 06978, South Korea. [6]National Center for Electron Microscopy, Molecular Foundry, Lawrence Berkeley National Laboratory, Berkeley, CA 94720, USA.
*These authors contributed equally to this work.
†Corresponding author. Email: jungwonpark@snu.ac.kr (J.P.); hans.elmlund@monash.edu (H.E.)

Downloaded from http://advances.sciencemag.org/ on January 30, 2021

GLC-EM data of colloidal metallic nanocrystals produced by distinct synthesis routes. Figure 1 provides a schematic overview of SINGLE. The SINGLE workflow is divided into two major steps: (i) preprocessing and (ii) particle 3D reconstruction. The preprocessing step operates on the movie frames of the time series. Each movie frame represents a 2D projection of several particles in random orientations. The following particle 3D reconstruction step operates on individual particle trajectories, each consisting of a set of differently projected views of a unique nanocrystal. We aim at providing the highest possible performance and efficiency on any CPU hardware, from supercomputers to workstations or even laptops. The SINGLE source code, as well as a large amount of introductory, tutorial, installation, usage, reference, and developer information, is available at simplecryoem.com. SINGLE is free software distributed under the GNU general public license, either version 3 of the license, or (at your option) any later version. The public git repository is available at https://github.com/hael/SIMPLE3.0.git.

The SINGLE workflow

First, time-window averaging over several frames with anisotropic motion correction is conducted, which improves the SNR versus the individual frames, leading to visible particles and substantially enhanced graphene signal in the power spectrum. Next, particle positions are manually identified in the first time window average, and these starting coordinates are inputted to the tracker. Following tracking, graphene background subtraction is done. Subsequently, time-restrained 2D clustering and in-plane registration are applied to identify the centers of mass of the particle views and remove the frames corresponding to the contiguous time segments where the particle has moved out of the narrow depth of focus of the aberration corrected TEM. Next, a starting model is generated on the basis of the expected crystallographic structure, particle diameter, and constituent elements. Last, 3D reconstructions are produced, atomic coordinates are fitted, and atomic-scale structure analyses, such as strain mapping, are performed.

Time-window averaging with anisotropic motion correction

In 2015, we published near-atomic resolution 3D reconstructions of two individual nanocrystals, obtained by combining GLC-EM with a method for ab initio single-particle 3D reconstruction for solving the inverse problem of recovering the unknown 3D orientations of the individual noisy nanocrystal projections (*17*). In that study, we had to apply moving window averaging over five consecutive movie frames to improve the SNR to a level that allowed successful 3D reconstruction. Since the nanocrystals are imaged rotating freely in liquid at ambient temperature, moving time-window averaging represents a potent risk for incoherent averaging and resolution loss. In our 2020 study (*18*), we improved the time-window averaging by including isotropic motion correction to account for stage drift. Furthermore, we included correlation-based frame weights to marginalize the influence of the flanking frames in the time window that often agreed poorly with the average due to motion of the nanocrystals, motion of the liquid, and deformation of the two graphene layers. To further correct for resolution loss due to anisotropic (beam-induced) motion, we here introduce weighted time-window averaging using an elastic deformation model to represent the beam-induced motions, as previously described (*19*).

Tracking of the individual particles throughout the time series

Our previous attempts at developing a method for tracking were based on correlating neighboring, systematically shifted windows in the time series. This worked well for a few particle trajectories, but the failure rate was too high (*17*, *18*). Here, we introduce a new tracking method based on translational registration of nonoverlapping time windows (30 frames by default) using fast Fourier transforms

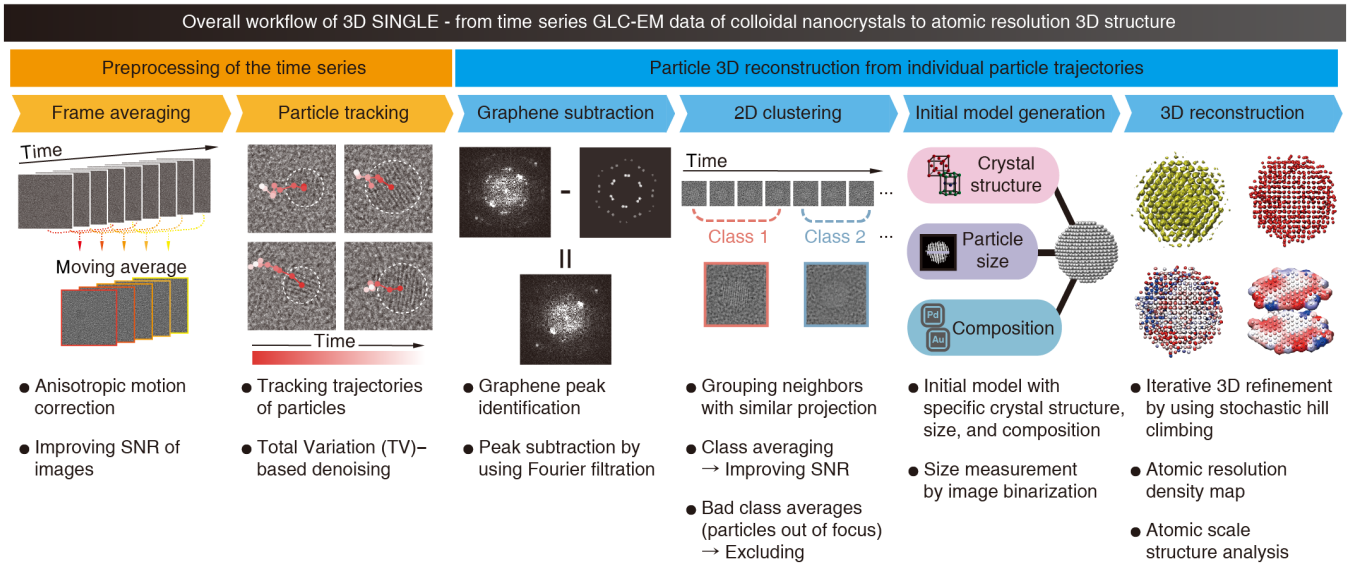

Fig. 1. Overall workflow of SINGLE. Overall workflow and descriptions of each step of SINGLE are shown. SINGLE consists of two major steps: Preprocessing of the time series (orange), including (i) time-window frame averaging with anisotropic motion correction and (ii) tracking particle trajectory with using total variation (TV)–based denoising, and particle 3D reconstruction from individual particle trajectories (blue), including (i) graphene background identification and subtraction, (ii) time-restrained 2D clustering with exclusion of out-of-focus images, (iii) initial model generation, and (iv) 3D reconstruction and atomic-scale structure analysis.

Downloaded from http://advances.sciencemag.org/ on January 30, 2021

(FFTs) and the phase correlation method in conjunction with interpolation of a quadratic function to identify a correlation maximum with subpixel accuracy (*20*). The extracted time windows are denoised using total variation (TV)–based denoising (*21*) and masked with a soft-edged spherical mask before obtaining shifts through iterative registration between the average over the time window, parameterized with respect to the shifts, and the individual particle views. TV denoising is based on the principle that noisy signals have high TV, i.e., the integral of the absolute gradient of the signal is high. Denoising is achieved through reducing this variation in a manner that preserves edges and structural features. We tested this algorithm on our previously published datasets (*17*, *18*). The combined use of denoising and time-averaging provided a robust method that enabled efficient tracking of the motion of the individual nanocrystals throughout the movie. Figure 2 shows the tracking trajectories for two representative nanocrystals, which could not be successfully reconstructed using our previous approach. Despite the inherent movement of the nanocrystals, sometimes bringing them out of the depth of focus, and the strong solvent background, the overall shape of the nanocrystal and/or crystalline features remain discernible, attesting to the robustness of the tracking algorithm. Notably, we were able to recover previously challenging trajectories and obtain their 3D reconstructions [see Fig. 2 (A and B) and fig. S1].

Graphene background subtraction

In comparison to conventional materials science TEM, where atomic resolution can be achieved through a single exposure of a thin electron transparent material, images of nanocrystals in a GLC have comparably low SNR due to the strong background introduced by the solvent and graphene of the liquid cell. In our two previous studies (*17*, *18*), the background of the GLC was modeled on the basis of the eight averages over the eight nearest neighbors of the particle image. The background subtraction was validated for each of the eight averages by inspecting the average power spectrum after subtraction and selecting the one with least pronounced graphene peaks. This worked well for a few particle trajectories. However, in many instances, honeycomb-like lattices showed up in the reconstructed 3D densities due to graphene bias. Through careful comparison of experimental and simulated particle trajectories, it became clear that the background is best modeled by two graphene sheets, rotated with respect to one another. Here, we introduce an automated Fourier filtration method for removing these peaks, preserving as much as possible of the information content related to the particle itself. Graphene subtraction is repeated as follows for each individual view of the particle trajectory (see Fig. 3A for schematic): 1)For each individual view, obtain the rotational average of the power spectrum over its eight nearest neighbors, each containing GLC background signal. Rotational averaging is performed over 60°, as constrained by the reciprocal hexagonal lattice of graphene, to reduce the influence of signals related to the particle and the solvent. 2)Calculate the rotational correlations of the generated spectrum with that of a theoretical graphene sheet. To further minimize the effect of noise and residual solvent background only the most prominent graphene resolution bands are included in this calculation (~2.1, 1.2, and 1.1 Å). The correlation profile unambiguously distinguishes two sets of correlation peaks corresponding to two graphene layers and identifies the location of the Fourier components to remove. 3)Mask away both sets of graphene peaks in the particle Fourier transform using a smooth polynomial function that is zero at each determined peak position and approaches one within less than three Fourier pixels. The background-subtracted particle trajectory is used in all subsequent image processing steps.

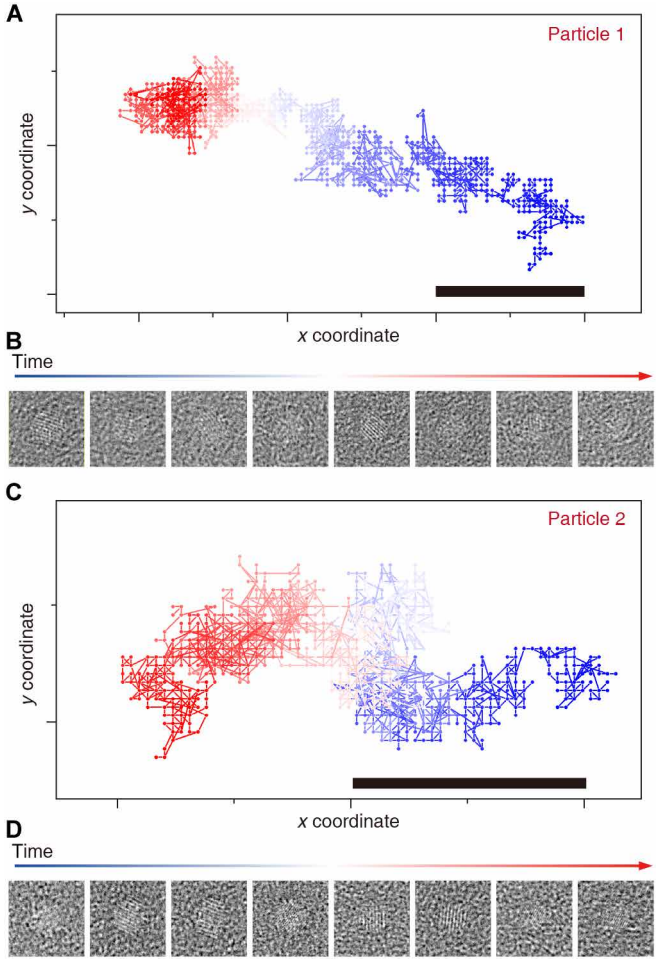

Fig. 2. Tracking of individual nanocrystal trajectories. Tracking results of particle 1 (**A** and **B**) and 2 (**C** and **D**) throughout the movie (blue to red). Representative time averages of raw unaligned particle images (50 frames) are shown (B and D). Scale bars, 1 nm.

We found this automated procedure efficiently removes the graphene bias in the 3D reconstructions as well as in the time-restrained class averages (see Fig. 3B). For different nanocrystal particle trajectories, the average relative rotations between the two graphene sheets and the standard deviations are not identical. This indicates that there are spatiotemporal variations in the GLC architecture, possibly due to corrugation of the graphene sheets forming the liquid pockets and the presence of multiple domains in the graphene sheets. Hence, it is necessary to model the graphene background on the level of the individual views of the particle trajectories.

Time-restrained 2D clustering and in-plane registration

Visual inspection of the images and power spectra of the time series data processed in our previous two studies (*17*, *18*) indicated that the orientation change during the image acquisition is not homogeneous. Orientation changes are rapid and often accompanied by a vertical movement in the solution that brings the nanocrystal out of the narrow depth of focus of the aberration-corrected TEM.

Downloaded from http://advances.sciencemag.org/ on January 30, 2021

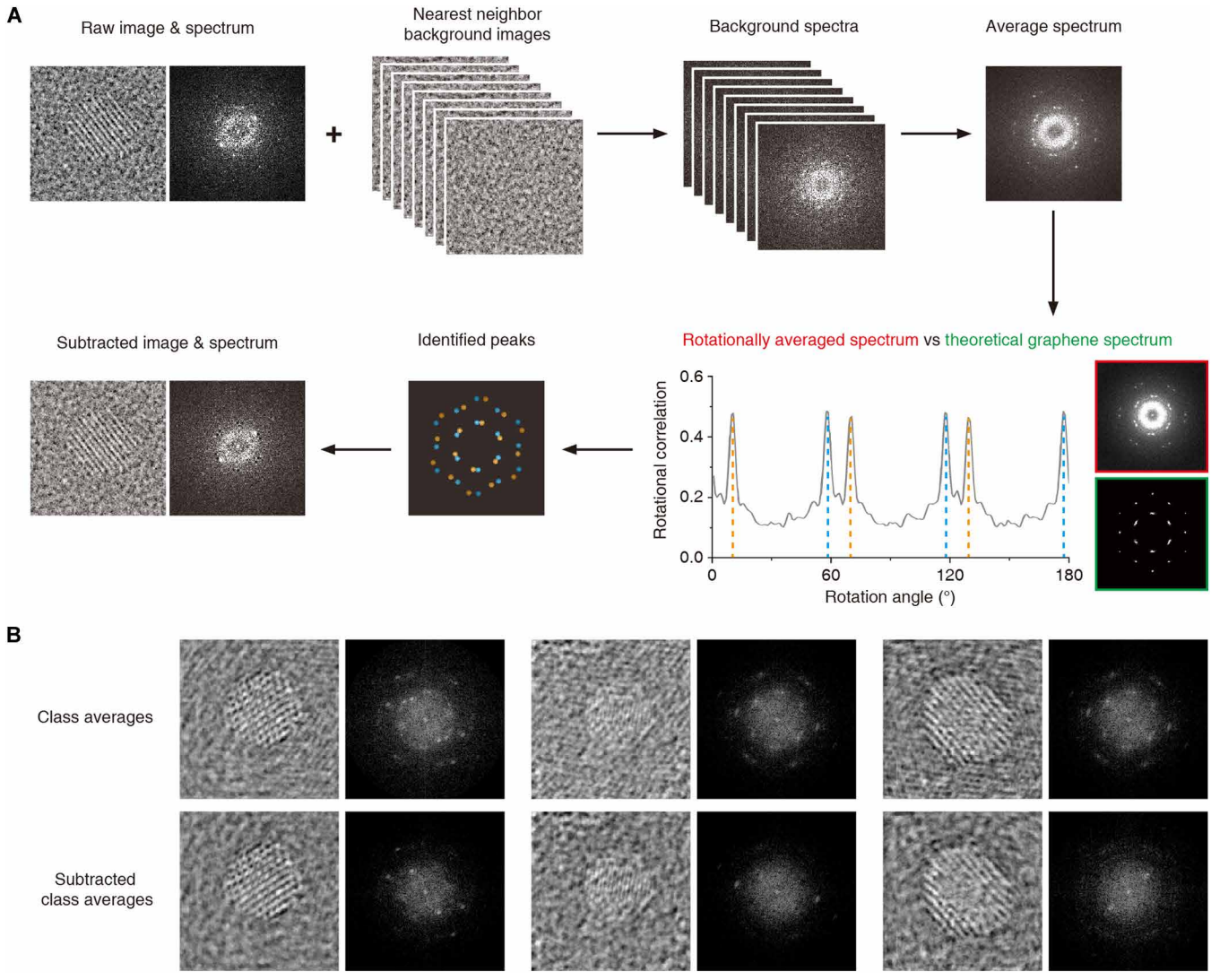

Fig. 3. Schematic depiction of the graphene subtraction procedure. (**A**) Graphene peak identification and subtraction. An average background spectrum is obtained from the eight nearest neighboring images of the GLC. Rotational averaging (increments of 60°) emphasizes the apparent signals of the reciprocal hexagonal lattices of the two graphene layers. Rotational correlations calculated between the averaged experimental (red) and theoretical graphene spectra (green) unequivocally identify the location of the graphene peaks of each layer (indicated orange and blue). The graphene peaks are subsequently masked out in the particle Fourier transform. (**B**) Representative class averages and their FFT images before and after graphene background subtraction.

Rotation of nanocrystals compartmentalized by a GLC is likely affected by the vertical confinement and interactions between the GLC and the passivating organic ligands. Here, we characterize the nature of the nanocrystal rotations in the highly confined space of the GLC by mapping the angular distance between neighboring views of a previously reconstructed particle trajectory (see Fig. 4A). Measuring the angular distance between neighboring views is a nontrivial problem, since the 3D reconstruction algorithm is probabilistic, i.e., one particle view is assigned a distribution of projection directions with weights (*10*, *22*). Therefore, we use a greedy algorithm to derive a lower bound of the rotational change by measuring the angular distance between the two closest projection directions of the neighboring distributions. The angular change plot for one of our previously reconstructed particles [referred to as particle 1 in our previous paper (*18*)] shows that changes in projection direction do not occur continuously between each frame within the 2.5-ms interval and include discrete stochastic events. Substantial (>5°) changes in projection direction occur in less than 10% of all frames. Furthermore, the rate of rotational change is higher in the beginning of the series and decreases toward the end, presumably due to drying of the solvent during the prolonged TEM imaging. Since rotational diffusion depends on the dimension of the embedding solution in the GLC, the orientation coverage for nanoparticles with different sizes and compositions can be manipulated by controlling the encapsulated volume of the liquid, the frame rate, and the electron dose rate. Our method for quantifying the changes in projection direction will be helpful for these kinds of analyses. The high degree of correlation between neighboring particle views along the time series explains why time-window averaging in conjunction with motion correction can be used so effectively to improve the SNR versus the individual frames. In previous single-particle cryo-EM studies, we have shown that 2D analysis can be a rapid and powerful

Downloaded from http://advances.sciencemag.org/ on January 30, 2021

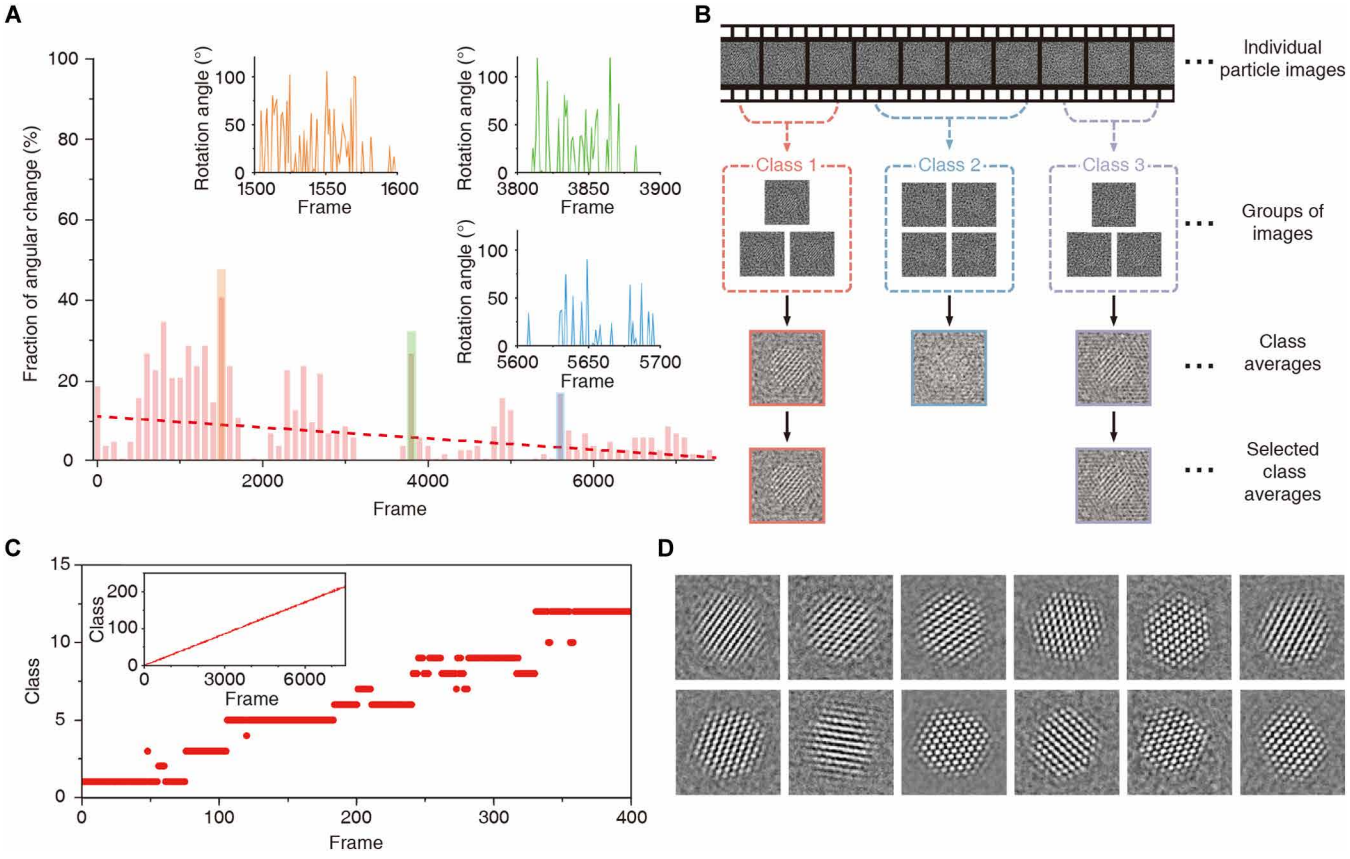

Fig. 4. Time-restrained 2D clustering. (**A**) Fraction of angular change throughout the time series. Red dashed line is the trend line. Projection directions are changing rapidly in the regions between frames 1500 to 1600 (orange), frames 3800 to 3900 (green), and frames 5600 to 5700 (blue). Insets are plots depicting angular difference in projection direction in those regions. (**B**) Schematic depiction of time-restrained 2D class averaging. (**C**) Plot showing allocated classes for individual frames in the 1 to 400 region. Inset is plot showing allocated classes over all frames. (**D**) Class averages obtained with time-restrained 2D clustering and alignment.

tool for obtaining SNR-enhanced class averages in an unsupervised manner (*23*, *24*). However, the method used for single-particle cryo-EM images, where there is no correlation between views along a trajectory in time, relies on combinatorial optimization through stochastic hill climbing with random initialization. This advanced method is not needed for the simpler task of analyzing nanocrystal particle trajectories. We therefore designed an algorithm where initialization is done in a time-dependent manner through defining the size of a window in time (35 frames by default) and creating mutually exclusive classes along the time dimension (see Fig. 4B). Figure 4C and its inset shows the relationship between frame order and assigned classes. The class boundaries are refined deterministically and iteratively by correlating each nanocrystal view with its current, preceding and succeeding class along the time trajectory, while maximizing the correlation over the three in-plane degrees of freedom. This deterministic approach thus operates in a substantially reduced search space and improves the accuracy of the cluster, rotation, and shift parameters obtained, ultimately improving the SNR versus the individual frames (see Fig. 4D).

Particle diameter estimation

The diameter of the particle is estimated from the class averages obtained as described above. A 2D version of Otsu's algorithm (*25*) is applied to distinguish between foreground and background pixels in the class averages. The longest distance between any two foreground pixels represents the diameter of the class average. The minimum of all class average diameters is taken as an estimate of the 3D particle diameter, assuming approximately spherical shape. In the case of nonspherical particles, we have found that the minimum diameter provides a better estimate of the diameter for starting model generation than for example the average or median diameter, because views along the smaller dimension tend to be better centered.

Starting model generation

The 2D projection images of the particle trajectories have a large degree of translational symmetry due to the high degree of crystallinity in the nanocrystal core. This explains why the reconstruction of an initial ab initio 3D density (as it is typically done in cryo-EM) often fails. The interfering background signal is also a contributing factor. Therefore, we developed a starting model estimation procedure that uses the knowledge that the particles have an approximately cubic atomic position arrangement with bond lengths similar to the bulk material. A starting model is estimated on the basis of the lattice configuration expected from the bulk material, using the cubic crystal system (primitive cubic, body-centered cubic, or face-centered cubic). The atomic coordinates of the lattice are used to fill the volume from the center and out to the estimated diameter. Next, atomic densities are simulated as described by Rullgård *et al.* (*26*), using

Downloaded from http://advances.sciencemag.org/ on January 30, 2021

5-Gaussian atomic scattering factors (*27*). 2D reprojections of this simulated 3D density represent well the character of the projections in the core of the nanocrystal and overcome the issues related to translational symmetry and interfering background signal.

3D reconstruction

The 3D refinement method used in biological cryo-EM cannot straightforwardly be applied to time series data of nanocrystals. Critical modifications had to be introduced.

• The Fourier shell correlation (FSC)–based estimation of the SNR and associated matched filter, as implemented for cryo-EM images (*10*, *11*), does not work for GLC-EM nanocrystal time series due to inflated resolution estimations in the early stages. Low-pass limited refinement is used instead, with a resolution limit that allows the atomic signals to participate in the projection matching (~1.5 Å) from the start. Contrary to protein molecules, low-resolution information of the nanocrystals does not convey the shape information necessary for convergence. Low-frequency information is also largely absent in the movies due to the image formation characteristics of the aberration-corrected HRTEM setup.

• It is not possible to use probabilistic, i.e., weighted, assignment of the in-plane rotations and origin shifts due to the high degree of translational symmetry of the nanocrystal 2D projections. Deterministic assignment of in-plane degrees of freedom is used instead.

In addition to these modifications, we use the starting model estimation procedure outlined above to provide an initial 3D reference. Furthermore, we use a two-stage refinement scheme, where a low-pass limit of 1.5 Å is typically used for the first 10 iterations to establish the correct shape of the nanocrystal and the following 10 to 20 iterations are low-pass limited to 1 Å to allow the atoms and their shapes to drive the 3D alignment. 3D density maps and corresponding atomic maps obtained using our new developments are shown in Fig. 5. Three nanocrystals of different sizes, which were not successfully reconstructed before, were selected for benchmarking (see fig. S1). 3D maps, fitted atomic maps, and radial strain maps are shown in Fig. 5 (A to C). Microscopic structural details at atomic level can be analyzed by using the atomic maps produced with our method. All interatomic distances along the <111>, <100>, and < 110> directions can be measured and plotted (see Fig. 5D). The plot shows marginal expansion of lattice parameters, which is consistent with previous results (*18*). Particle size versus lattice parameter expansion is plotted in Fig. 5E. Adding three additional data points obtained from this study to our previously reported results (*18*) establishes a weak negative correlation between nanocrystal size and lattice parameter expansion. Detailed strain analysis (Fig. 5F) and unit cell structure analysis (Fig. 5G) are also possible using the atomic maps generated with our method.

Validation of the 3D reconstructions

We previously demonstrated that our stochastic 3D reconstruction algorithm is robust to initial model bias (*22*), which is less of a concern for this kind of images that have much higher SNR than cryo-EM images. We generated a model of a disordered nanocrystal by molecular dynamics simulation to assess whether SINGLE is applicable to highly disordered nanocrystals. The simulated disordered particle has a twin plane and disorder in multiple atomic positions. In the multislice simulations, we applied translational motion and random defocus variations (±5 nm) to represent realistic particle motion. The 3D density map of the disordered nanocrystal obtained from 5000 simulated images with SNR = 0.1 and a starting model with perfect crystalline order agreed excellently with the original particle (see Fig. 6A), demonstrating that the reconstruction algorithm is robust to initial model bias. Furthermore, the fact that the refined 3D reconstructions obtained from experimental data show facets, structural degeneracies, lattice parameter deviations, internal defects, and strain (*18*) that are absent in the starting volumes are strong evidence that the final maps are correct (see Fig. 6B). The correlation between reprojections of the map and the experimental images was plotted versus iteration. The plot shows that the starting model fits the data poorly but nevertheless provides a good starting 3D registration, as indicated by the massive jump in correlation in the first few iterations (see Fig. 6C).

The standard validation techniques used in cryo-EM [gold-standard FSC (*28*) and tilt-pair validation (*29*)] are not applicable because of the nature of the GLC-EM nanocrystal time series data and the 3D reconstruction approach used. The most important validation step is to ensure that the reprojections of the final map agree with the views of the particle trajectory. This comparison is made difficult by the strong GLC solvent background signal, causing the individual particle views to have low SNR compared to the corresponding reprojections of the 3D reconstruction. Therefore, we developed a validation method that uses the time-restrained 2D class averages that have high SNRs—well suited for visual inspection—and importantly were generated independently of any 3D model. Our validation procedure works as follows: the converged 3D reconstruction is used as a starting point for five iterations of 3D refinement using the time-restrained class averages. The resulting validation 3D map obtained using the class averages provides the opportunity to compare reprojections with class averages that have substantially higher SNR than the individual nanocrystal views (see Fig. 6D).

To quantify the degree of similarity between the validation 3D reconstruction obtained from class averages and the final 3D map obtained using the individual views of the particle trajectories, we calculated the real space correlation between the map pairs, resulting in correlations of better than 0.9. As expected, the smallest nanocrystal (particle 2) with the highest degree of disorder and the least favorable accumulative SNR (fewest particles included) gave rise to the lowest-quality 3D reconstruction. Nevertheless, the reprojections of the validation 3D reconstruction agreed excellently with the class averages for particle 2 (see Fig. 6D, second panel), and we see no reason to dismiss its atomic structure. More careful inspection of class averages versus reprojections revealed that the only substantial discrepancies occurred at the surface of the nanocrystals. This is likely due to dynamic effects confined to the solvent accessible surface and can be explained by the fact that the class averages capture the particle in a restricted window in time, whereas the reprojections are generated using a 3D reconstruction obtained through averaging over the entire time series. Resolving this kind of surface localized dynamic effects will be the subject of our future studies.

Distribution of the projection directions of the rotating nanocrystals is important for the validity and quality of the 3D reconstruction. Production of 3D maps with high resolution and precision requires sufficient coverage of projection directions. To inspect the distribution of the projection directions assigned by the 3D reconstruction process, we created an atomic representation in which each atomic position represents a projection direction colored according to time (see Fig. 6E). If the same projection direction is sampled multiple times, it receives the color of the latest direction. Particles

Downloaded from http://advances.sciencemag.org/ on January 30, 2021

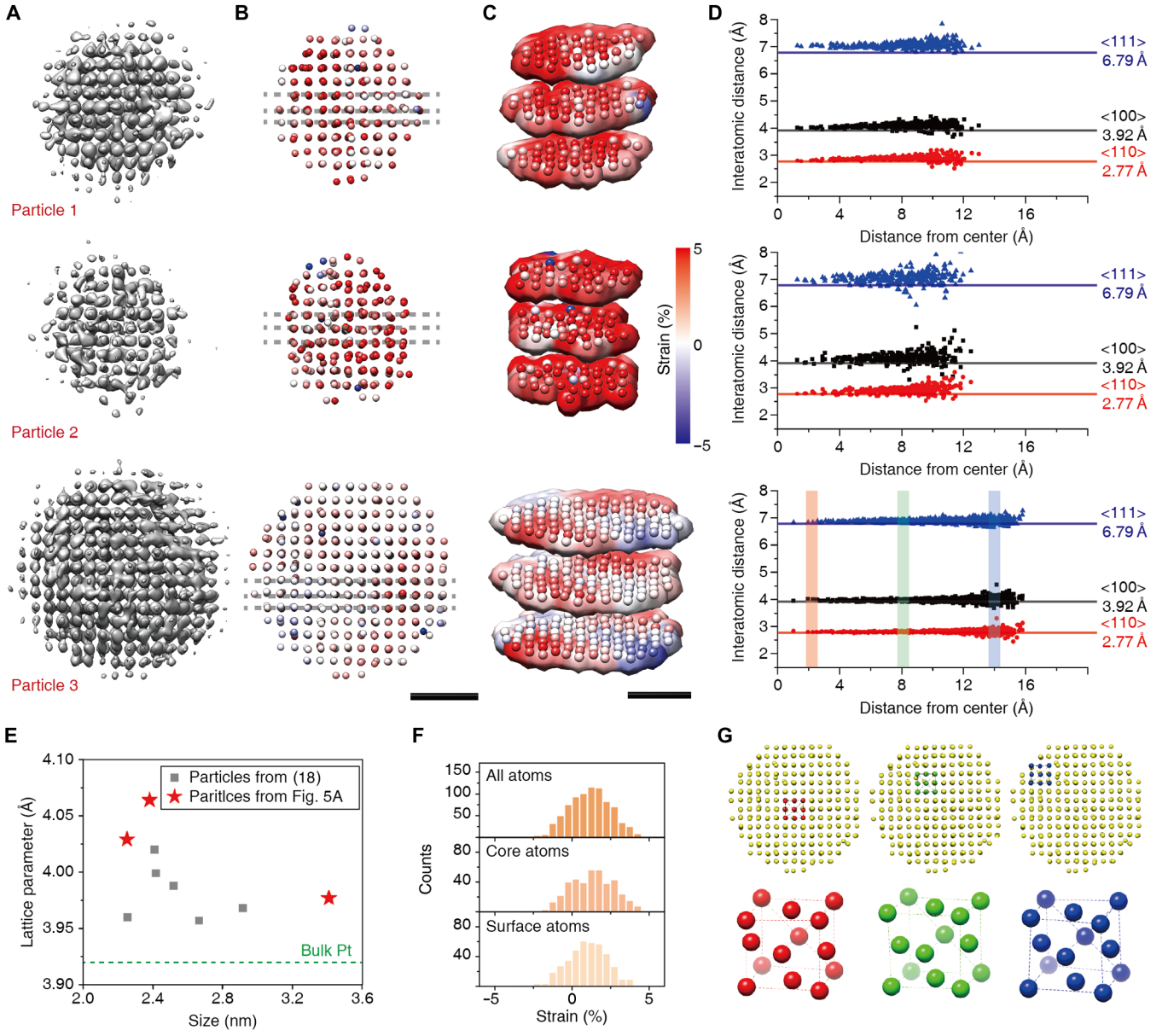

Fig. 5. 3D reconstruction results and atomic level structure analysis. (**A** to **C**) 3D density maps (A), radial strain maps from fitted atomic coordinates (B), and their slice representation (C). (**D**) Interatomic distances in the directions of <110> (red), <100> (black), and < 111> (blue) for three nanocrystals. (**E**) Fitted lattice parameters of previously reported nanocrystals (*18*) (gray squares) and new results (red stars). (**F**) Histogram of radial strain of all atoms (top), core atoms (middle), surface atoms (bottom) of particle 3. (**G**) Unit cell structure of core (red), middle (green), and surface (blue) of particle 3. Scale bars, 1 nm.

1 and 3 had the best projection direction coverage. Particle 2 showed the most random distribution of projection directions. Analyzing the projection direction distribution can also help understanding nanocrystal rotation in GLC. Particles 1, 2, and 3 showed evidence of precession, i.e., change in the orientation of the rotational axis of the rotating nanocrystal, because the projection directions tended to cluster in ring patterns. How the actual atomic structures of the nanocrystals affect the rotational dynamics will require further study and analysis of many more particle trajectories. However, our results indicate that the larger the nanocrystal, the more restricted its rotations, presumably because the rotational dynamics of larger particles are more influenced by the GLC confinement.

DISCUSSION

In conclusion, we have demonstrated that the computational methods in SINGLE can be used to obtain atomic-resolution nanocrystal density maps. Currently, our 3D reconstruction algorithm assumes that the individual views of the particle trajectory conform to the projection-slice theorem (*30*). A valid concern, given this assumption, is that diffraction contrast and/or multiple scattering may introduce artefacts when reconstructing large particles. We previously demonstrated that Pt nanocrystals of up to 4 nm in diameter can be successfully reconstructed (*18*). 3D reconstruction of larger nanocrystals (>4 nm) would be more challenging due to their slower rotation rate, causing poor rotational coverage. We also previously

Downloaded from http://advances.sciencemag.org/ on January 30, 2021

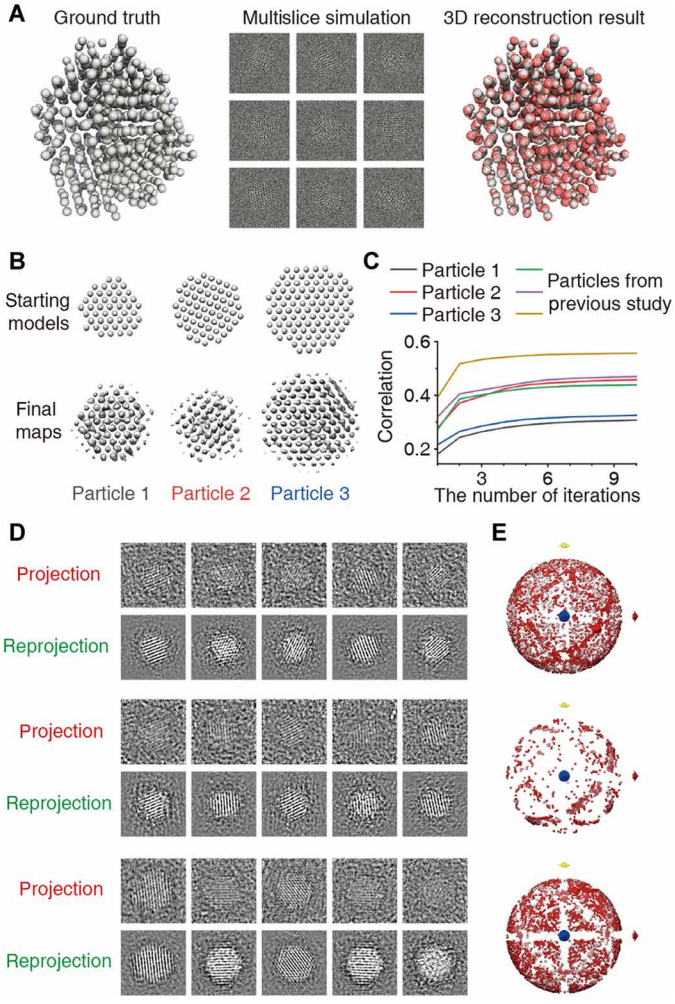

Fig. 6. Validation of 3D reconstructions. (**A**) 3D reconstruction of simulated disordered particle with known atomic structure. Left: Model of a disordered nanocrystal obtained by molecular dynamics simulation. Middle: 5000 multislice simulated images with noise added to give a SNR = 0.1. Right: Atomic map (red) as result of 3D reconstruction overlaid with the ground truth model (gray). (**B**) Starting 3D models and final 3D density maps obtained from experimental data. (**C**) Correlation between reprojections of the refined 3D density map and the experimental particle views plotted as a function of iteration for the first stage of 3D refinement. Particles presented in this paper (black, red, and blue color) and presented in a previous study (*18*) (green, purple, and ocher color) are plotted. (**D**) Comparison of class averages (indicated as projection) with reprojections for validation of the three structures. (**E**) Time-dependent atomic representation of the projection directions for the three structures: white (beginning) to pink (middle) to red (end). Red, yellow, and blue arrows indicate *x*, *y*, and *z* axes, respectively.

demonstrated through 3D reconstruction of multislice simulated images of Ag and Ni (a light-element transition metal) nanocrystals that SINGLE is widely applicable to nanocrystals with homogeneous atomic composition (*18*). Using an advanced liquid cell configuration, such as a GLC with ordered nanochambers allowing control of the liquid thickness (*31*, *32*), would extend the applicability of SINGLE since the liquid thickness is an important factor for efficient data acquisition (fig. S2). In conclusion, the SINGLE suite we introduce in this study along with GLC-EM of colloidal nanocrystals provides an efficient analytical platform to understand the structural origin of the unique physical and chemical properties of nanocrystals in their native solution phase.

MATERIALS AND METHODS

Synthesis of Pt nanocrystals

Pt nanocrystals of 2 to 3 nm in diameter were synthesized by mixing 0.05 mmol $(NH_4)_2Pt(II)Cl_4$ (99.995%; Sigma-Aldrich), 0.75 mmol tetramethylammonium bromide (98%; Sigma-Aldrich), 1 mmol of polyvinylpyrrolidone (M.W. 29,000; Sigma-Aldrich), and 10 ml of ethylene glycol in a three-neck round bottom flask. The mixture was heated to 160°C and kept at 160°C for 20 min. After cooling the solution to room temperature, 90 ml of acetone was added to precipitate the particles. The product was centrifuged at 4000 rpm for 5 min. The supernatant was discarded, and the Pt nanocrystals were redispersed in 5 mM Hepes buffer solution with pH 7.4.

Preparation of GLCs

Graphene was synthesized on 25-μm-thick copper foil (99.8%; Alfa Aesar) by the chemical vapor deposition method. The copper foil in a quartz tube was heated to 1000°C for 30 min in hydrogen environment. Graphene was grown onto the copper foil with flows of 25 cm^3/min of methane and 10 cm^3/min of hydrogen at 1000°C. After 20 min, the product was rapidly cooled to room temperature with methane flow. Graphene TEM grids were prepared by transferring the graphene to a holey carbon grid using the direct transfer method. The graphene covered copper foil was treated with weak oxygen plasma to etch the graphene on one side of the foil. A Quantifoil grid (Ted Pella) was placed onto the other grid side, on which graphene was not etched. Next, the copper foil substrate was etched with ammonium persulfate aqueous solution (0.1 g/ml). The graphene grid was washed with deionized water several times. The GLC was fabricated with two graphene grids. Pt nanocrystal solution (0.5 μl) was loaded onto a graphene grid. The other graphene grid was gently laid on the graphene grid with the liquid sample, so that the liquid sample was sandwiched between the two graphene sheets. Sealing of the liquid sample is accomplished through the strong interaction between the two graphene surfaces.

Acquisition of TEM images

TEM movies of Pt nanocrystals in the GLC were obtained at a rate of 400 frames per second using TEAM I, an FEI Titan 80/300 TEM equipped with a postspecimen geometric- and chromatic-aberration corrector and a Gatan K2 IS direct electron detector. Thousands of images with 1920 × 1728 pixels and 0.358 Å pixel resolution were acquired at a dose rate of ~17 e−/pixel·frame or below at an acceleration voltage of 300 kV. The pixel size was confirmed on the basis of the known lattice spacing of the graphene sheets containing the nanocrystals. TEM images of rotating nanocrystals were used in the 3D reconstruction process. Successful 3D reconstruction of nanoparticles that differ in size, composition, and solvating molecules requires extensive optimization of imaging conditions, image processing, and reconstruction parameters. TEM imaging conditions must be optimized to obtain good SNR of the 2D projected lattice for a given rotational rate, local thickness of the liquid, and image capture rate.

SUPPLEMENTARY MATERIALS

Supplementary material for this article is available at http://advances.sciencemag.org/cgi/content/full/7/5/eabe6679/DC1

Downloaded from http://advances.sciencemag.org/ on January 30, 2021

REFERENCES AND NOTES

1. R. J. D. Miller, Femtosecond crystallography with ultrabright electrons and x-rays: Capturing chemistry in action. *Science* **343**, 1108–1116 (2014).
2. A. Baldi, T. C. Narayan, A. L. Koh, J. A. Dionne, In situ detection of hydrogen-induced phase transitions in individual palladium nanocrystals. *Nat. Mater.* **13**, 1143–1148 (2014).
3. M. A. Pfeifer, G. J. Williams, I. A. Vartanyants, R. Harder, I. K. Robinson, Three-dimensional mapping of a deformation field inside a nanocrystal. *Nature* **442**, 63–66 (2006).
4. M. Cargnello, V. V. T. Doan-Nguyen, T. R. Gordon, R. E. Diaz, E. A. Stach, R. J. Gorte, P. Fornasiero, C. B. Murray, Control of metal nanocrystal size reveals metal-support interface role for ceria catalysts. *Science* **341**, 771–773 (2013).
5. M. Azubel, J. Koivisto, S. Malola, D. Bushnell, G. L. Hura, A. L. Koh, H. Tsunoyama, T. Tsukuda, M. Pettersson, H. Häkkinen, R. D. Kornberg, Nanoparticle imaging. Electron microscopy of gold nanoparticles at atomic resolution. *Science* **345**, 909–912 (2014).
6. W. Gao, P. Tieu, C. Addiego, Y. Ma, J. Wu, X. Pan, Probing the dynamics of nanoparticle formation from a precursor at atomic resolution. *Sci. Adv.* **5**, eaau9590 (2019).
7. F. Bertolotti, D. N. Dirin, M. Ibáñez, F. Krumeich, A. Cervellino, R. Frison, O. Voznyy, E. H. Sargent, M. V. Kovalenko, A. Guagliardi, N. Masciocchi, Crystal symmetry breaking and vacancies in colloidal lead chalcogenide quantum dots. *Nat. Mater.* **15**, 987–994 (2016).
8. A. Kim, S. Zhou, L. Yao, S. Ni, B. Luo, C. E. Sing, Q. Chen, Tip-patched nanoprisms from formation of ligand islands. *J. Am. Chem. Soc.* **141**, 11796–11800 (2019).
9. S. H. W. Scheres, RELION: Implementation of a Bayesian approach to cryo-EM structure determination. *J. Struct. Biol.* **180**, 519–530 (2012).
10. C. F. Reboul, S. Kiesewetter, M. Eager, M. Belousoff, T. Cui, H. De Sterck, D. Elmlund, H. Elmlund, Rapid near-atomic resolution single-particle 3D reconstruction with SIMPLE. *J. Struct. Biol.* **204**, 172–181 (2018).
11. T. Grant, A. Rohou, N. Grigorieff, *cis*TEM, user-friendly software for single-particle image processing. *eLife* **7**, e35383 (2018).
12. A. Punjani, J. L. Rubinstein, D. J. Fleet, M. A. Brubaker, cryoSPARC: Algorithms for rapid unsupervised cryo-EM structure determination. *Nat. Methods* **14**, 290–296 (2017).
13. J. M. Bell, M. Chen, P. R. Baldwin, S. J. Ludtke, High resolution single particle refinement in EMAN2.1. *Methods* **100**, 25–34 (2016).
14. D. Maluenda, T. Majtner, P. Horvath, J. L. Vilas, A. Jiménez-Moreno, J. Mota, E. Ramírez-Aportela, R. Sánchez-García, P. Conesa, L. del Caño, Y. Rancel, Y. Fonseca, M. Martínez, G. Sharov, C. A. García, D. Strelak, R. Melero, R. Marabini, J. M. Carazo, C. O. S. Sorzano, Flexible workflows for on-the-fly electron-microscopy single-particle image processing using *Scipion*. *Acta Crystallogr D Struct Biol* **75**, 882–894 (2019).
15. M. Khoshouei, M. Radjainia, W. Baumeister, R. Danev, Cryo-EM structure of haemoglobin at 3.2Å determined with the Volta phase plate. *Nat. Commun.* **8**, 16099 (2017).
16. A. Bartesaghi, C. Aguerrebere, V. Falconieri, S. Banerjee, L. A. Earl, X. Zhu, N. Grigorieff, J. L. S. Milne, G. Sapiro, X. Wu, S. Subramaniam, Atomic resolution cryo-EM structure of β-galactosidase. *Structure* **26**, 848–856.e3 (2018).
17. J. Park, H. Elmlund, P. Ercius, J. M. Yuk, D. T. Limmer, Q. Chen, K. Kim, S. H. Han, D. A. Weitz, A. Zettl, A. P. Alivisatos, Nanoparticle imaging. 3D structure of individual nanocrystals in solution by electron microscopy. *Science* **349**, 290–295 (2015).
18. B. H. Kim, J. Heo, S. Kim, C. F. Reboul, H. Chun, D. Kang, H. Bae, H. Hyun, J. Lim, H. Lee, B. Han, T. Hyeon, A. P. Alivisatos, P. Ercius, H. Elmlund, J. Park, Critical differences in 3D atomic structure of individual ligand-protected nanocrystals in solution. *Science* **368**, 60–67 (2020).
19. S. Q. Zheng, E. Palovcak, J.-P. Armache, K. A. Verba, Y. Cheng, D. A. Agard, MotionCor2: Anisotropic correction of beam-induced motion for improved cryo-electron microscopy. *Nat. Methods* **14**, 331–332 (2017).
20. H. S. Stone, M. T. Orchard, E.-C. Chang, S. A. Martucci, A fast direct Fourier-based algorithm for subpixel registration of images. *IEEE Trans. Geosci. Remote Sens.* **39**, 2235–2243 (2001).
21. L. I. Rudin, S. Osher, E. Fatemi, Nonlinear total variation based noise removal algorithms. *Physica D.* **60**, 259–268 (1992).
22. H. Elmlund, D. Elmlund, S. Bengio, PRIME: Probabilistic initial 3D model generation for single-particle cryo-electron microscopy. *Structure* **21**, 1299–1306 (2013).
23. C. F. Reboul, F. Bonnet, D. Elmlund, H. Elmlund, A stochastic hill climbing approach for simultaneous 2D alignment and clustering of cryogenic electron microscopy images. *Structure* **24**, 988–996 (2016).
24. C. F. Reboul, M. Eager, D. Elmlund, H. Elmlund, Single-particle cryo-EM-Improved ab initio 3D reconstruction with SIMPLE/PRIME. *Protein Sci.* **27**, 51–61 (2018).
25. N. Otsu, A threshold selection method from gray-level histograms. *IEEE Trans. Sys. Man. Cyber.* **9**, 62–66 (1979).
26. H. Rullgård, L.-G. Ofverstedt, S. Masich, B. Daneholt, O. Oktem, Simulation of transmission electron microscope images of biological specimens. *J. Microsc.* **243**, 234–256 (2011).
27. L.-M. Peng, G. Ren, S. L. Dudarev, M. J. Whelan, Robust parameterization of elastic and absorptive electron atomic scattering factors. *Acta Crystallogr. A* **52**, 257–276 (1996).
28. S. H. W. Scheres, S. Chen, Prevention of overfitting in cryo-EM structure determination. *Nat. Methods* **9**, 853–854 (2012).
29. P. B. Rosenthal, R. Henderson, Optimal determination of particle orientation, absolute hand, and contrast loss in single-particle electron cryomicroscopy. *J. Mol. Biol.* **333**, 721–745 (2003).
30. R. N. Bracewell, Strip integration in radio astronomy. *Aust J Phys* **9**, 198–217 (1956).
31. K. Lim, Y. Bae, S. Jeon, K. Kim, B. H. Kim, J. Kim, S. Kang, T. Heo, J. Park, W. C. Lee, A large-scale array of ordered graphene-sandwiched chambers for quantitative liquid-phase transmission electron microscopy. *Adv. Mater.* **32**, 2002889 (2020).
32. D. J. Kelly, M. Zhou, N. Clark, M. J. Hamer, E. A. Lewis, A. M. Rakowski, S. J. Haigh, R. V. Gorbachev, Nanometer resolution elemental mapping in graphene-based TEM liquid cells. *Nano Lett.* **18**, 1168–1174 (2018).

Acknowledgments

Funding: J.P. acknowledges Institutes for Basic Science (IBS-R006-D1), the National Research Foundation of Korea (NRF) grant funded by the Korea government (MSIT) (nos. NRF-2017R1A5A1015365 and NRF-2019M3E6A1064877), the MOTIE (Ministry of Trade, Industry & Energy), and KSRC (Korea Semiconductor Research Consortium) support program for the development of future semiconductor devices (no. 10080657). B.H.K., J.H., S.Kim, and J.P. acknowledge support by Samsung Science and Technology Foundation under project number SSTF-BA1802-08 for the development of the reconstruction algorithm. H.E. acknowledges the Australian Research Council (ARC) grant DP170101850 and the National Health and Medical Research Council, Australia, grant APP1125909. C.F.R. acknowledges Early Career Fellowship (APP1122769). The experiments were performed at the Molecular Foundry, Lawrence Berkeley National Laboratory, which is supported by the U.S. Department of Energy under contract no. DE-AC02-05CH11231. **Author contributions:** Conception/design of the work: C.F.R., J.H., P.E., J.P., and H.E. Software design: C.F.R., C.M., S.Kiesewetter, D.E., and H.E. All authors contributed to acquisition, analysis, and interpretation of data and writing of the manuscript. **Competing interests:** The authors declare that they have no competing interests. **Data and materials availability:** All data needed to evaluate the conclusions in the paper are present in the paper and/or the Supplementary Materials. Additional data related to this paper may be requested from the authors.

Submitted 6 September 2020
Accepted 10 December 2020
Published 29 January 2021
10.1126/sciadv.abe6679

Citation: C. F. Reboul, J. Heo, C. Machello, S. Kiesewetter, B. H. Kim, S. Kim, D. Elmlund, P. Ercius, J. Park, H. Elmlund, SINGLE: Atomic-resolution structure identification of nanocrystals by graphene liquid cell EM. *Sci. Adv.* **7**, eabe6679 (2021).

Downloaded from http://advances.sciencemag.org/ on January 30, 2021

Science Advances

SINGLE: Atomic-resolution structure identification of nanocrystals by graphene liquid cell EM

Cyril F. Reboul, Junyoung Heo, Chiara Machello, Simon Kiesewetter, Byung Hyo Kim, Sungin Kim, Dominika Elmlund, Peter Ercius, Jungwon Park and Hans Elmlund

Sci Adv **7** (5), eabe6679.
DOI: 10.1126/sciadv.abe6679

ARTICLE TOOLS http://advances.sciencemag.org/content/7/5/eabe6679

SUPPLEMENTARY MATERIALS http://advances.sciencemag.org/content/suppl/2021/01/25/7.5.eabe6679.DC1

REFERENCES This article cites 32 articles, 6 of which you can access for free
http://advances.sciencemag.org/content/7/5/eabe6679#BIBL

PERMISSIONS http://www.sciencemag.org/help/reprints-and-permissions

Use of this article is subject to the Terms of Service

Science Advances (ISSN 2375-2548) is published by the American Association for the Advancement of Science, 1200 New York Avenue NW, Washington, DC 20005. The title *Science Advances* is a registered trademark of AAAS.

Copyright © 2021 The Authors, some rights reserved; exclusive licensee American Association for the Advancement of Science. No claim to original U.S. Government Works. Distributed under a Creative Commons Attribution NonCommercial License 4.0 (CC BY-NC).

Downloaded from http://advances.sciencemag.org/ on January 30, 2021